Effect of Tank Diameter on Solid Suspension in Industrial Reactor Vessels

D. K. Iyer and A. K. Patel†

Department of Civil Engineering, National Institute of Technology Warangal, Warangal, Telangana-506004, India

†Corresponding Author Email: akpcivil@nitw.ac.in

ABSTRACT

Present research study analyses the suitability of baffled reactor vessels with large diameter agitated using the Rushton Turbine (RT) impeller maintained at standard clearance condition for the solid-liquid suspension process. The mean and turbulent flow fields associated with reactor vessels of various diameter were simulated using Computational Fluid Dynamics (CFD) approach. The impeller rotation was modelled using Multiple Reference Frame (MRF) technique and entrainment of air was simulated using Volume of Fluid (VOF) method respectively. The increase in the diameter of reactor vessel keeping impeller at standard clearance condition lead to the transition from double to single loop pattern with considerable decrease in the power number. In large reactor vessels, a low pressure zone is developed below the impeller which deflects the discharge streams and trailing vortices towards bottom surface of the reactor vessel causing the formation of single loop down-pumping pattern. The downward propagation of trailing vortices weaken the flow separation region behind the impeller blades which in turn decreases the form drag and power number of the impeller. The development of single loop down-pumping pattern, high magnitudes of axial velocity, vortex and turbulence fields near vessel bottom and inferior entrainment of air makes the large reactor vessels suitable for the solid-liquid suspension process. The high magnitudes of axial velocity developed below the impeller of large reactor vessel with same power consumption as compared to low clearance vessel makes the former vessel configuration more suitable for the solid-liquid suspension process.

1. INTRODUCTION

Suspension of fine solid particles in the liquid phase is one of the major unit operations associated with chemical, metallurgical, biochemical, pharmaceutical, food and petroleum industries. It is regarded that about 50% of the processes associated with various industries deal with suspension of solid particles in the liquid (Jirout & Jiroutová, 2020). Mechanically stirred reactor vessels with baffle walls are mainly employed for this purpose (Zhu et al., 2019). In these industries, reaction products and/or catalysts are suspended in the reagent to increase the rate of heat and mass transfer, to avoid settling of particles, to prepare liquid emulsions and to obtain uniform concentration gradient throughout the entire reactor vessel (Yapici et al., 2008). The design of reactor vessels for solid-liquid suspension process requires the determination of the just suspended speed

(N_{js}) or minimum agitation speed of the impeller which makes the solid particles suspend in the liquid without allowing them to settle down in the bottom surface of the vessel for higher duration of time (ie, more than 1s) (Armenante et al., 1998). The impellers rotated at speeds less than N_{js} fail to efficiently utilize the interfacial contact area or surface area and impellers rotated at speeds more than N_{js} decrease the rate of increase of heat and mass transfer associated with the dissolution and ion exchange processes (Armenante & Nagamine, 1998).

The N_{js} for the solid suspension process depends up on the geometric, operational and physical parameters of the vessel. Significant efforts have been made in the past to develop empirical correlations for predicting the N_{js} by various researchers (Zwietering, 1958; Kolář, 1961; Armenante et al., 1998; Armenante & Nagamine, 1998). According to the correlation provided by Zwietering (1958), N_{js} is affected by geometric parameters such as

NOMENCLATURE

B	width of baffle wall	i, j, k	co-ordinate directions
b	height of blade	k	turbulent kinetic energy
C_p	pressure coefficient	l	width of blade
$C_{1\varepsilon}, C_{2\varepsilon}, C_{3\varepsilon}, C_\mu$	model constants	$\dot{m}_{pq}$	mass transfer from p^{th} phase to q^{th} phase
D	diameter of RT impeller	$\dot{m}_{qp}$	mass transfer from q^{th} phase to p^{th} phase
d	diameter of reactor vessel	N	impeller speed
e	gas hold-up	N_{js}	just suspended speed
F_σ	surface tension force	N_{pt}	power number based on impeller torque
F_B	body forces (coriolis and centrifugal forces)	$N_{p\varepsilon}$	power number based on volume integrated turbulence dissipation rate
F_g	gravitational force	P'	power drawn
G_k	generation of turbulent kinetic energy from mean velocity gradients	p	mean pressure
G_b	generation of turbulent kinetic energy from buoyancy	p, q	phases
H	height of liquid in the absence of gas	Q	Q-criterion
H_D	height of liquid in presence of gas	r	distance to axis of vessel
h	impeller clearance	R	radius of vessel
i, j, k	co-ordinate directions	R_e	Reynolds number
S_k, S_ε	user defined source terms	u_r	radial velocity
$S_{\alpha q}$	mass source term	u_{tip}	impeller tip velocity
$\|S\|$	Euclidean norm of strain rate tensor	u_q	velocity of qth phase
t	time	$\|w\|$	Euclidean norm of rotation rate tensor
u	velocity of flow	x, y, z	Cartesian co-ordinates
u_a	axial velocity	Y_M	contribution of fluctuating dilatation in compressible turbulence to the overall turbulence dissipation rate
Greek Symbols			
α	volume fraction	γ	energy imbalance
α_q	volume fraction of qth phase	μ	dynamic viscosity of fluid
ε	turbulent dissipation rate	δ_{ij}	Kronecker delta
ρ_q	density of a fluid phase q under consideration	$\sigma_k, \sigma_\varepsilon$	turbulent Prandtl numbers
$-\rho_q \overline{u_i' u_j'}$	Reynolds stress	μ_t	turbulence viscosity
ω	turbulence eddy frequency	Ω	angular speed of impeller

distance of the impeller from bottom surface of the vessel (ie, impeller clearance) and the diameter of the reactor vessel. The standard configuration of the reactor vessel having impeller at one-third height of the tank was widely used for majority of the unit operations associated with various industries (Deglon & Meyer, 2006). However, N_{js} was found to decrease with decrease in the clearance of the impeller in the reactor vessels (Harriott, 1962). Kolář (1961) and Zwietering (1958) have not properly considered the disc type impellers while deriving the correlations, whereas Nienow (1968) employed the Rushton Turbine (RT) impeller to analyse the effect of impeller clearance on the particle suspension. Nienow (1968) found that decrease in the impeller clearance causes transition from normal double re-circulation pattern to single re-circulation pattern which leads to the reduction of N_{js} for the solid suspension in the reactor vessels. Conti et al. (1981) have also arrived at similar conclusions for low clearance vessels. The flow pattern transition has eventually resulted in 25%-30% reduction in the impeller power number (Montante et al., 1999; Yapici et al., 2008) and

16.37% reduction in the mixing time (Ochieng et al., 2008; Ochieng & Onyango, 2008) respectively. The critical impeller clearance causing double loop to single loop pattern transition and flow features associated with the single loop pattern were analysed by various scholars such as Conti et al. (1981), Galletti et al. (2003), Li et al. (2011), Montante et al. (1999, 2001), Ochieng et al. (2008) and Zhu et al. (2019) respectively. Moreover, increase in the speed of rotation of the impeller under low clearance condition has not produced any changes in the single loop pattern (Li et al., 2011; Zhu et al., 2019). On the other hand, large impellers under low clearance condition has developed double re-circulation pattern instead of single re-circulation pattern (Zhu et al., 2019). The physical reasons causing the transition from double re-circulation pattern to single re-circulation pattern and associated reduction in the impeller power number were explained in detail by Iyer and Patel (2022).

Even though, the low clearance vessel is a suitable configuration for the solid-liquid suspension process, the excessive wear and tear of the impeller is a burning issue faced by the industrial practitioners (Sepro mixing &

pumping, 2020). The impact of solid particles on the impeller blades located near the bottom surface of the reactor vessel causes erosion of the blade material (surface wear) resulting in the decrease of the thickness of the impeller blades (Jirout & Jiroutová, 2020). The material erosion commences from the leading edge of the blades and progress towards the disc region causing overall change in the geometric shape of the impeller (shape wear) (Jirout & Jiroutová, 2020). The surface wear and shape wear eventually decrease the strength, pumping efficiency and other performance characteristics of the impeller. Moreover, blending time of the reactor vessel increases with progressive wear and tear of the impeller blades. Thus, the wear and tear of impeller blades increase the maintenance cost of the industries and in extreme situations, complete replacement of the impeller becomes necessary for uninterrupted operation of the reactor vessel (Jirout & Jiroutová, 2020).

Therefore, geometric configurations of the reactor vessel suitable for suspending solid particles without causing wear and tear of impeller blades need to be determined. In this regard, the present study proposes to analyse the suitability of reactor vessels with large diameter keeping RT impeller at standard clearance condition for the solid-liquid suspension process. Since, the RT impeller is placed at standard clearance condition, its contact with solid particles decreases which in turn leads to less wear and tear of the impeller blades. This hypothesis is developed from the intuitions that the N_{js} depends on the vessel diameter apart from the impeller clearance (Zwietering, 1958) and the presence of large space between the impeller and vessel boundary can lead to single loop down-pumping pattern rather than double loop pattern (Zhu et al., 2019). Although, Zwietering (1958) has provided empirical relationships for determining the N_{js} under various configurations of the reactor vessel, flow field characteristics and performance features which eventually determine the suitability of a reactor vessel configuration for the solid-liquid suspension process (Montante et al., 2001; Zhu et al., 2019) weren't evaluated.

Thus, the main objective of the present research study is to analyse the suitability of large diameter reactor vessels with RT impeller at standard clearance condition for the solid-liquid suspension process using the CFD approach. The mean and turbulent flow field characteristics as well as the performance goals of reactor vessels with large diameter were analysed to assess the suitability of the same for the solid-liquid suspension process. Moreover, the hydrodynamic reasons causing flow pattern transition and variations in the performance goals such as impeller power number and gas hold-up with increase in the diameter of the standard reactor vessel are also elucidated in the present research study.

2. REACTOR CONFIGURATIONS

The cylindrical reactor vessels of various diameter (d) were considered for the present research work. The water and air were considered as the working fluids and the water was filled up to a height (H) of 0.27m in the

reactor vessel. A six-bladed RT impeller with a diameter (D) around $\frac{d}{3}$ was concentrically mounted at a clearance (h) of $\frac{H}{3}$ from the bottom surface of the reactor vessel. The RT impeller is established as the optimal type of impeller for solid-liquid suspension process as it provides appropriate flow fields (Montante et al., 1999), minimum particle suspension velocity and efficient usage of power supplied to the impeller (Nienow, 1968). Thus, the RT impeller is considered for the analyses in the present research study. The RT impeller was rotated at a speed of 200 rpm so as to generate the turbulent flow fields corresponding to R_e=29000. Each blade has a width (l) of $\frac{D}{4}$ and a height (b) of $\frac{D}{5}$ respectively. Four equally spaced baffle walls of width (B) of $0.1d$ were extended throughout the entire height of the reactor vessel. The diameter of the reactor vessel is expressed in the non-dimensional form as $\frac{d}{D}$ and varied in the range between 2.58-4.30 so as to analyse the impact of $\frac{d}{D}$ on the flow fields and performance goals of the reactor vessel. The sectional elevation of one of the reactor vessel having diameter of 0.27m (i.e., standard configuration) is shown in Fig. 1 and the numerical values of various geometric parameters adopted for the present research study are provided in Table 1.

3. COMPUTATIONAL METHODOLOGY

The CFD approach was used to predict the mean and turbulent flow fields associated with the agitated reactor vessels in the present study. The CFD approach provides detailed characterisation of flow fields with less time and cost as compared to the experimental techniques (Oberkampf & Trucano, 2002; Joshi et al., 2011). Moreover, proper instrumentation facilities are not yet
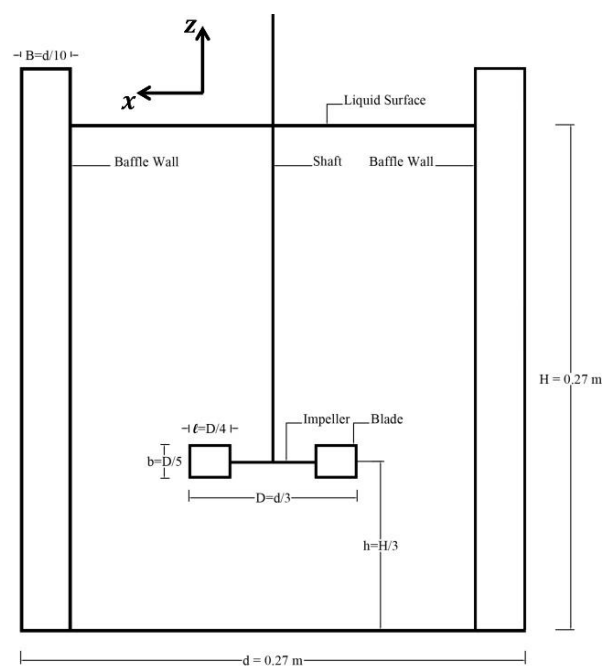
Fig. 1 Sectional elevation of the standard reactor vessel agitated using RT impeller

Table 1 Summary of reactor vessel configurations

Reactor vessel parameter	Mathematical definition	Dimension (m)
Diameter of reactor vessel (d)	_	0.24-0.40
Height of liquid (H)	_	0.27
Width of baffle walls (B)	$\dfrac{d}{10}$	0.027
Diameter of impeller (D)	$\dfrac{d}{3}$	0.093
Clearance of impeller (h)	$\dfrac{H}{3}$	0.093
Speed of impeller (N)	_	200 rpm
Width of impeller blade (l)	$\dfrac{D}{4}$	0.02325
Height of impeller blade (b)	$\dfrac{D}{5}$	0.0186

developed to accurately measure the local turbulent quantities near the impeller even from advanced experimental techniques (Alcamo et al., 2005). Further, the CFD approach is appropriate for the present study since the objective is to assess the viability of reactor vessels with large diameter for the solid-liquid suspension process which requires testing of large number of reactor vessel configurations. However, this task will be cumbersome and costly with the experimental techniques (Joshi et al., 2011). Also, it is well established that the CFD approach with systematic and scientific Verification and Validation (V&V) process provides reliable and accurate predictions of the mean and turbulent flow fields (Freitas, 2002; Oberkampf & Trucano, 2002; Celik et al., 2008; Coroneo et al., 2011).

Verification is the process of systematic minimisation of various sources of numerical error associated with the CFD model whereas validation is the process of comparison of the predictions from the CFD approach with the corresponding results from the experimental techniques (Oberkampf & Trucano, 2002). In the present study, numerical verification is performed by the grid independence study of all the reactor vessel configurations as well as employing higher order discretization schemes, numerical schemes, well established modelling approach and boundary conditions respectively. The validation is done by comparing the mean and turbulent flow field predictions from the standard configuration of the reactor vessel with the corresponding results from the experimental studies.

The three dimensional single phase and multiphase CFD models were developed using commercially available ANSYS FLUENT 17.0 software. The Reynolds Averaged Navier Stokes approach which is widely adopted for modelling the agitated reactors (Deglon & Meyer, 2006; Coroneo et al., 2011; Joshi et al., 2011) was considered for the present research study. The standard $k - \varepsilon$ model was used to resolve the Reynolds stress terms in the governing equations. Although, various turbulence models such as Spalart-Allmaras, Shear Stress Transport, $k - \omega$ and Reynolds Stress

Models were used for simulating the turbulent flows in the agitated reactors, the standard $k - \varepsilon$ model has provided accurate predictions (Alonzo-Garcia et al., 2019) for a wide range of flow problems at a reasonable cost and hence considered for the present research study. The rotation of the RT impeller was simulated using the pseudo-steady Multiple Reference Frame (MRF) technique since it maintains an appropriate balance between the accuracy of predictions and computational cost (Deglon & Meyer, 2006; Coroneo et al., 2011). In the MRF method, governing equations are solved in a rotating frame of reference near the impeller and in a stationary frame of reference near the periphery of the reactor vessel and are adequately coupled at the interface separating the rotating and stationary zones. The entrainment of air into the reactor vessel was modelled using the implicit Volume of Fluid (VOF) method (Hirt & Nicholas, 1981) and the surface tension was included into the VOF model using Continuum Surface Force (CSF) model. The continuity and momentum equations were coupled using SIMPLE scheme and the resulting equations were discretized using second order upwind scheme. During the VOF simulations, volume fraction and pressure terms were discretised using Geo-Reconstruct scheme and PRESTO scheme respectively. The details of standard $k - \varepsilon$ model, VOF method, MRF impeller modeling scheme, pressure-velocity coupling schemes and the numerical discretization schemes are elucidated in ANSYS (2013).

The Reynolds-averaged continuity and momentum equations, which are expressed in the Cartesian tensor form (ANSYS, 2013), are given in Eqs. (1-2) respectively:

$$\frac{\partial \rho_q}{\partial t} + \frac{\partial (\rho_q u_i)}{\partial x_i} = 0 \tag{1}$$

$$\frac{\partial (\rho_q u_i)}{\partial t} + \frac{\partial (\rho_q u_i u_j)}{\partial x_j} = -\frac{\partial p}{\partial x_i} + \frac{\partial}{\partial x_j}\left[\mu\left\{\frac{\partial u_i}{\partial x_j} + \frac{\partial u_j}{\partial x_i} - \frac{2}{3}\delta_{ij}\frac{\partial u_k}{\partial x_k}\right\}\right] + \frac{\partial (-\rho_q \overline{u_i' u_j'})}{\partial x_j} + F_\sigma + F_B + F_g \tag{2}$$

Where ρ_q is the density of fluid (q represents the phase under consideration), u is the velocity of flow, p is the pressure, μ is the viscosity of fluid, δ_{ij} is the Kronecker delta ($\delta_{ij} = 1$ if $i = j$ and $\delta_{ij} = 0$ if $i \neq j$), $-\rho_q \overline{u_i' u_j'}$ is the Reynolds stress, F_σ is the surface tension force, F_B is the body force and F_g is the gravitational force. The term t specifies time, x represents the spatial coordinate and the subscripts i, j, k indicate the three coordinate directions, respectively.

The Reynolds stress present in Eq. (2) contains the product of fluctuating velocity terms, which is converted into mean velocity gradients using the Boussinesq hypothesis (ANSYS, 2013), as given in Eq. (3):

$$-\rho_q \overline{u_i' u_j'} = \mu_t \left[\frac{\partial u_i}{\partial x_j} + \frac{\partial u_j}{\partial x_i} \right] - \frac{2}{3} \left[\rho_q k + \mu_t \frac{\partial u_k}{\partial x_k} \right] \delta_{ij} \quad (3)$$

Where μ_t is the turbulence viscosity which is calculated using one or two equation turbulence models. In the standard $k - \varepsilon$ model, μ_t is represented as the function of turbulent kinetic energy (k) and turbulence dissipation rate (ε), as given in Eq. (4), while the additional transport equations for calculating the k and ε are given in Eqs. (5-6), respectively:

$$\mu_t = \rho_q C_\mu \frac{k^2}{\varepsilon} \quad (4)$$

$$\frac{\partial(\rho_q k)}{\partial t} + \frac{\partial(\rho_q k u_i)}{\partial x_i} = \frac{\partial}{\partial x_j} \left[\left(\mu + \frac{\mu_t}{\sigma_k} \right) \frac{\partial k}{\partial x_j} \right] + G_k + G_b - \rho_q \varepsilon - Y_M + S_k \quad (5)$$

$$\frac{\partial(\rho_q \varepsilon)}{\partial t} + \frac{\partial(\rho_q \varepsilon u_i)}{\partial x_i} = \frac{\partial}{\partial x_j} \left[\left(\mu + \frac{\mu_t}{\sigma_\varepsilon} \right) \frac{\partial \varepsilon}{\partial x_j} \right] + C_{1\varepsilon} \frac{\varepsilon}{k} (G_k + C_{3\varepsilon} G_b) - C_{2\varepsilon} \rho_q \frac{\varepsilon^2}{k} + S_\varepsilon \quad (6)$$

Where σ_k and σ_ε are turbulent Prandtl numbers, G_k and G_b indicate the generation of turbulent kinetic energy from mean velocity gradients and buoyancy, respectively. The Y_M specifies the contribution of fluctuating dilatation in compressible turbulence to the overall turbulence dissipation rate. Finally, S_k and S_ε are the user-defined source terms while $C_{1\varepsilon}$, $C_{2\varepsilon}$, $C_{3\varepsilon}$ and C_μ are the model constants. The default values of these model constants were found through experiments and the same are given below:

$C_{1\varepsilon} = 1.44$, $C_{2\varepsilon} = 1.92$, $C_\mu = 0.09$, $\sigma_k = 1.0$ and $\sigma_\varepsilon = 1.3$

The values of these model constants have worked well for various types of turbulent flows (ANSYS, 2013) and were thus adopted for the present research study.

The term F_B comprises of Coriolis and centrifugal forces which are generated due to the rotation of the impeller. The expression of F_B is given in Eq. (7).

The term F_B is considered for the calculations only when the governing equations are solved in a rotating frame of reference in the MRF method.

$$F_B = \left(-2\rho_q \Omega \times u_i \right) - \left(-\rho_q \Omega \times \{ \Omega \times x \} \right) \quad (7)$$

Where Ω is the angular speed of the impeller.

Water and air are respectively regarded as the primary and secondary (dispersed) phases for the numerical simulations. The interfaces between the air and water phases are tracked by solving an additional continuity equation for the volume fraction of each phase under consideration. The continuity equation for the volume fraction of the qth phase is given in Eq. (8):

$$\frac{1}{\rho_q} \left[\frac{\partial}{\partial t} (\alpha_q \rho_q) + \nabla \cdot (\alpha_q \rho_q \overline{u_q}) = S_{\alpha q} + \sum_{p=1}^{n} (\dot{m}_{pq} - \dot{m}_{qp}) \right] \quad (8)$$

Where $\dot{m}_{pq}$ is the mass transfer from the pth phase to the qth phase, $\dot{m}_{qp}$ is the mass transfer from the qth phase to the pth phase, $S_{\alpha q}$ is the mass source term of qth phase, α_q is the volume fraction of the qth phase in a computational cell and u_q is the velocity of the qth phase. The volume fraction α of any phase is defined as given in Eq. (9). According to the value of α in each computational cell, corresponding properties of fluid and variables are assigned to each computational cell. The sum of volume fractions of various phases in any computational cell equals unity.

$$\alpha = \begin{cases} 1 & Liquid \\ 0 & Gas \\ 0 < \alpha < 1 & Interface \end{cases} \quad (9)$$

In the present research study, the interface between the phases is depicted when the value of α is equal to 0.50. The above-mentioned volume fraction equation is solved for the dispersed phases and the volume fraction of the primary phase is computed using Eq. (10).

$$\sum_{q=1}^{n} \alpha_q = 1 \quad (10)$$

The computational domain comprising of reactor vessel, RT impeller and baffle walls were properly discretized using the finite volume based grids as shown in Fig. 2. The computational domain is divided mainly into two regions such as a cylindrical region surrounding the impeller and a region outside this inner cylindrical region. The cylindrical region surrounding the impeller was discretized using tetrahedral elements and the region outside this cylindrical region was discretized using the hexahedral elements. The tetrahedral elements were adopted for discretizing the inner cylindrical region since these elements have the capability to define the complex shape of the RT impeller with less effort and time (Longest & Vinchurkar, 2007). The region outside the inner cylindrical region was further divided into various sub-regions and discretized with hexahedral elements. The hexahedral elements were adopted for these sub-regions outside the inner cylindrical region since the sub-regions have simpler geometries and the hexahedral elements provide accurate flow field predictions with less computational cost (Longest & Vinchurkar, 2007). In each of the sub-region, particular care was taken to align the grid elements in the predominant direction of flow so as to resolve the sharp flow gradients associated with each sub-region (Vinchurkar & Longest, 2008). The computational grid adopted for the present study can be called as 'hybrid grid' since the tetrahedral and hexahedral elements are appropriately arranged and

Table 2 Details of the grids used for grid independence study of the standard reactor vessel

Grid	Element size of impeller (m)	Overall number of elements	Overall number of nodes
Grid 1	0.004	300573	304574
Grid 2	0.0008	996072	361096
Grid 3	0.00035	4497937	1325522
Grid 4	0.000258	7418360	2329381
Grid 5	0.00024	8451837	2607928
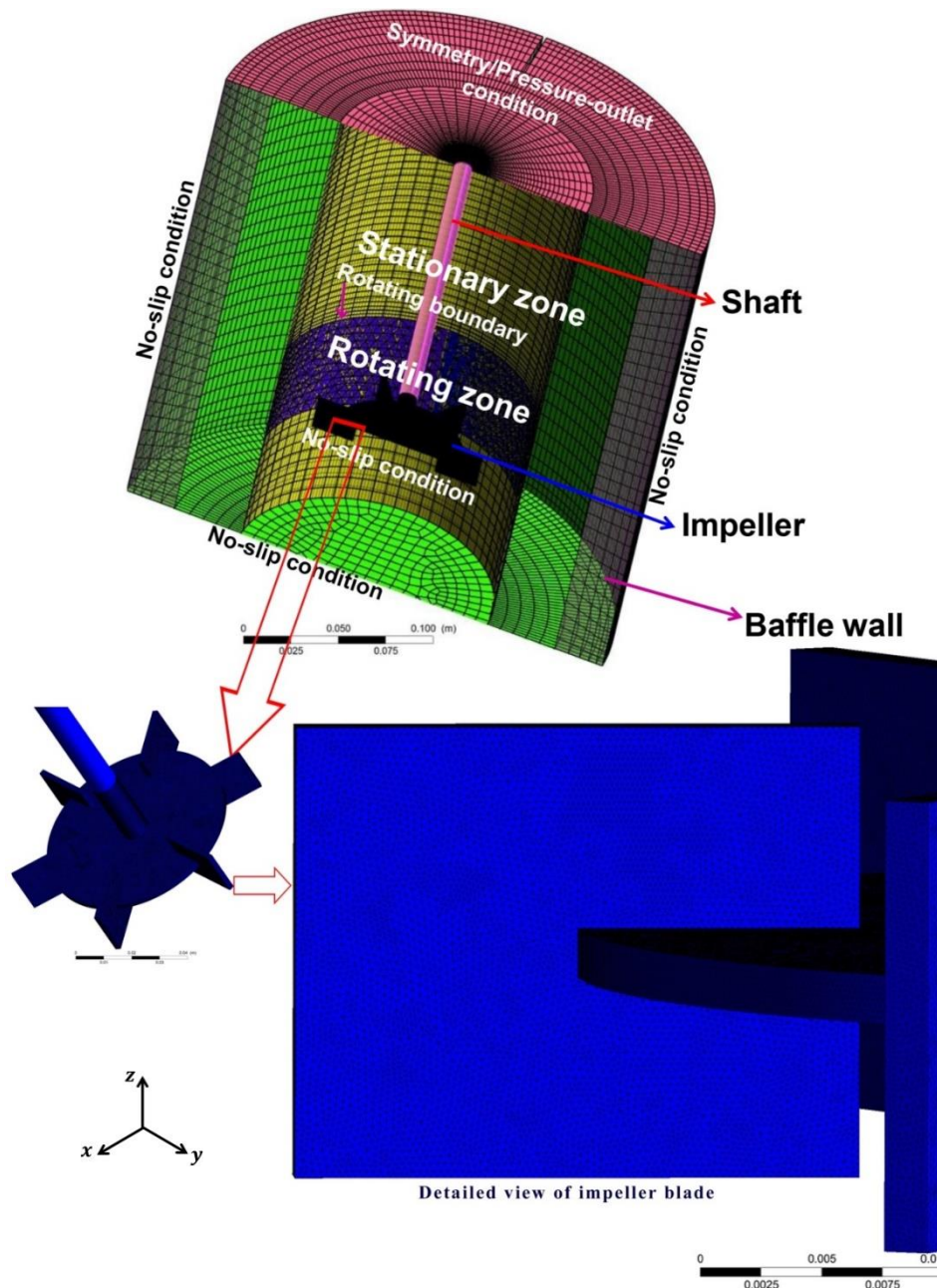
Fig. 2 Computational grid developed

oriented so as to obtain accurate flow field predictions with less computational cost.

Five grids of significantly different resolution were generated for each reactor vessel configuration for the grid independence study by refining the size of the elements comprising the impeller. The details of the grids generated for the grid independence study of the standard reactor vessel configuration are given in Table 2. The thickness of RT impeller and baffle walls were adequately included in the finer grids generated for each reactor vessel configuration. The impeller surfaces, baffle walls, bottom surface of the vessel and periphery of the vessel were represented as solid surfaces with no-slip

boundary condition. On the other hand, top surface of the reactor vessel was specified using symmetry boundary condition during the single phase simulations and pressure-outlet condition during the multiphase simulations respectively.

The major performance goals associated with the reactor vessel such as power number based on impeller torque (N_{pt}), power number based on volume integrated turbulence dissipation rate $(N_{p\varepsilon})$ and gas hold-up (e) were considered for the present research study. The gas hold-up denotes the oxygen transfer into the reactor vessel. The relative difference between N_{pt} and $N_{p\varepsilon}$ is indicated as energy imbalance (γ) (Başbuğ et al., 2018) which is considered as an important parameter for evaluating the grid independence conditions of the various reactor vessel configurations.

The expressions for calculating N_{pt}, $N_{p\varepsilon}$, γ and gas hold-up are given in the Eqs. (11-14) respectively.

$$N_{pt} = \frac{P^{'}}{\rho_q N^3 D^5} \tag{11}$$

Where $P^{'} = 2\pi N\tau$, $P^{'}$ indicates the impeller power drawn, τ is the net torque on the impeller blades and ρ_q is the density of fluid under consideration.

$$N_{p\varepsilon} = \frac{\iiint \rho_q \varepsilon dV}{\rho_q N^3 D^5} \tag{12}$$

Where ε is the turbulent dissipation rate.

$$\gamma = \frac{N_{pt} - N_{p\varepsilon}}{N_{pt}} \tag{13}$$

$$e = \frac{H_D - H}{H_D} \tag{14}$$

Where H_D and H are the height of the liquid in the presence of the gas as well as in the absence of the gas respectively. The gas hold-up is represented as percentage values.

A convergence criteria of 10^{-6} was adopted for the residuals of all the variables associated with the governing equations. Moreover, the convergence of performance goals such as N_{pt} and $N_{p\varepsilon}$ were constantly

monitored during the simulations. The simulations were stopped when the residuals of all the variables reduced below the convergence criteria adopted and the performance goals becomes constant for large number of iterations in a particular simulation. The simulations were performed in a workstation having double precision 64 bit Intel (R) Xeon (R) E5-1620 3.6 GHz processor with 12 cores.

4. RESULTS AND DISCUSSION

4.1 Grid Independence Study and Validation

The standard configuration of the reactor vessel was considered for the grid independence study since the results from several experimental and computational studies are available for the validation purposes. Figure 3(a) illustrates the variation of N_{pt} and $N_{p\varepsilon}$ with grid resolution while the Fig. 3(b) shows the variation of axial profile of normalized radial velocity $\left(\frac{u_r}{u_{tip}}\right)$ with the grid resolution. The $\frac{u_r}{u_{tip}}$ is considered for the grid independence study as the flow field developed by the standard reactor vessel is strongly radial in nature (Van Der Molen & Van Maanen, 1978). It is clear from Figs. 3(a) and 3(b) that N_{pt} and $\frac{u_r}{u_{tip}}$ increases from Grid-1 to Grid-3 and becomes constant thereafter whereas $N_{p\varepsilon}$ significantly increases from Grid-1 to Grid-4 and provides negligible variation with Grid-5. Also, the numerical error represented in the form of Grid Convergence Index (GCI) was found to be less than 5% for these flow variables under consideration. Thus, the flow field results from the Grid-4 are independent of grid resolution and can be considered for the validation purpose. Since, the mean and turbulent flow fields become independent of grid resolution with Grid-4 and the numerical error associated with the same is very less, the mean and turbulent flow fields predicted from the present CFD model are reliable and the same CFD methodology can be employed for modelling the reactor vessels with various diameter. The grid independence study was performed in a similar manner for

---: Experimental study (Bates et al., 1963), ●: N_{pt}, ◆: $N_{p\varepsilon}$, —●—: Experimental study (Wu & Patterson, 1989), ●●●●●: Grid 1, ▬ ▬ ▬: Grid 2, — ·· —: Grid 3, — · —: Grid 4, ▬▬▬: Grid 5

(a)   (b)

Fig. 3 Variations of (a) N_{pt} and $N_{p\varepsilon}$ and (b) axial profile of $\frac{u_r}{u_{tip}}$ close to the impeller with grid resolution
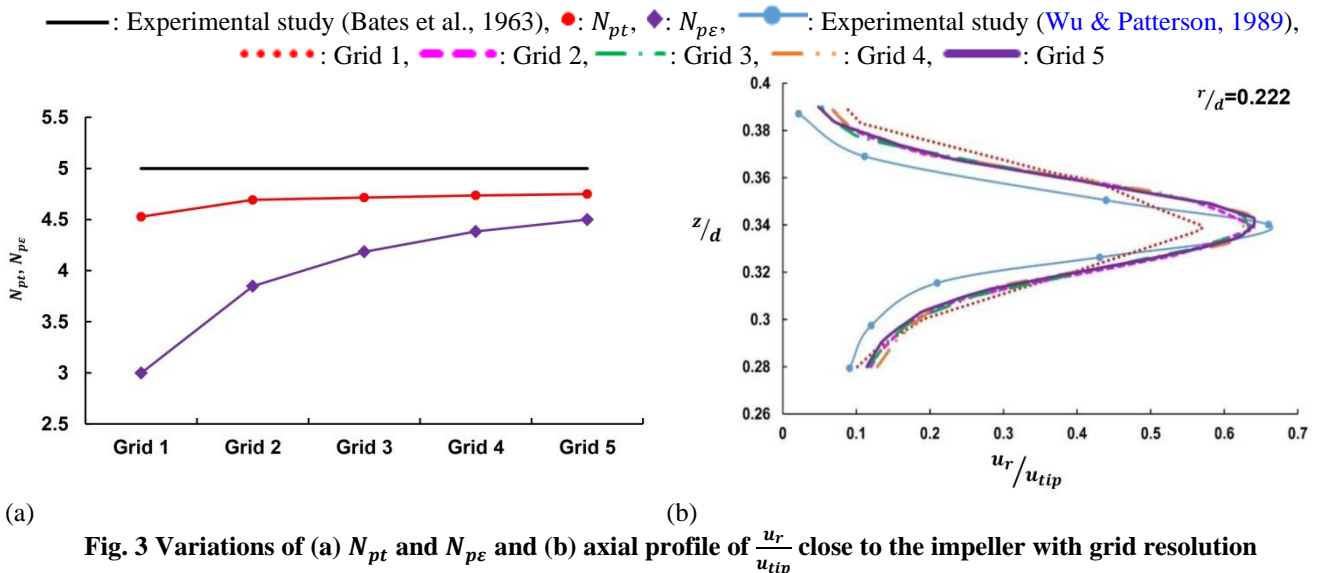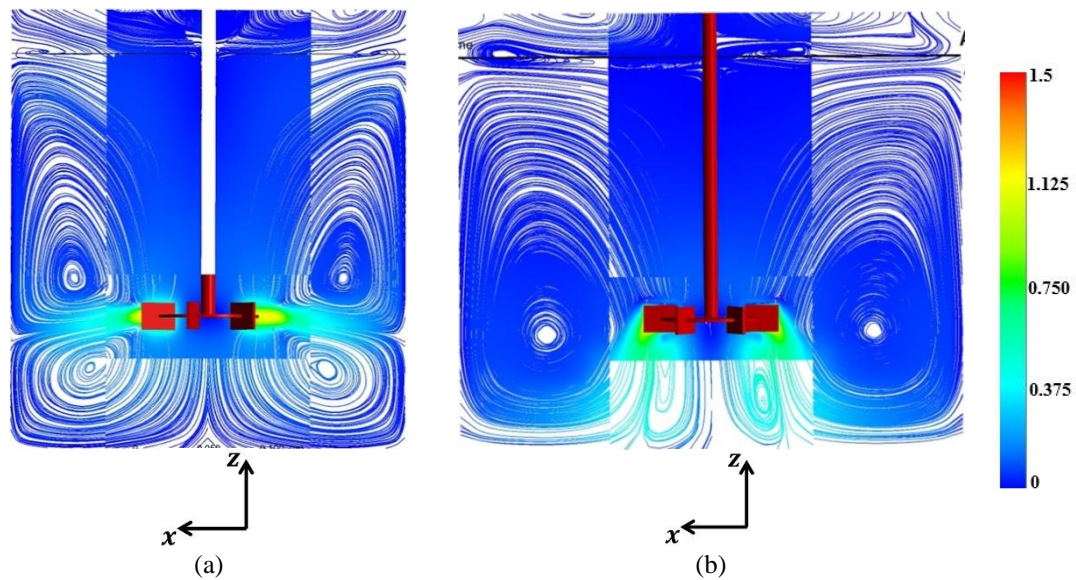
Fig. 4 Flow patterns associated with the $\frac{d}{D}$ of (a) 2.90 (standard reactor vessel) and (b) 4.30 (large reactor vessel) (Black line in the figures indicate air-water interface before the commencement of simulations)

the remaining reactor vessel configurations (ie, reactor vessels with larger and smaller diameters).

The predictions of N_{pt}, $N_{p\varepsilon}$ and $\frac{u_r}{u_{tip}}$ from Grid-4 were compared with the corresponding results from the experimental studies of Bates et al. (1963) and Wu and Patterson (1989) respectively as a part of validation process. The N_{pt} and $N_{p\varepsilon}$ were accurately predicted with errors less than 5% and 10% respectively. The axial profile of $\frac{u_r}{u_{tip}}$ obtained from the present CFD model is very close to the corresponding experimental profile and the magnitude and location of peak $\frac{u_r}{u_{tip}}$ were accurately predicted. Moreover, the γ obtained from the present CFD model was only 5.3% while the past research works (Joshi et al., 2011; Karpinska & Bridgeman, 2018) have reported much higher magnitudes of the same (more than 20%) in their CFD models. Thus, the grid resolution obtained from the grid independence study of the present CFD model is adequate for the accurate prediction of various flow field parameters associated with the reactor vessel. The small percentage errors associated with the predictions of N_{pt}, $N_{p\varepsilon}$, γ and axial profile of $\frac{u_r}{u_{tip}}$ elucidate that the present CFD methodology is capable of accurately predicting the mean and turbulent flow field characteristics related with the agitated reactor vessel. Hence, this CFD methodology can be confidently employed for predicting the flow fields associated with the reactor vessels having various diameter.

In short, the present CFD methodology with systematic V&V process can provide accurate flow field predictions from the reactor vessel configurations of various diameter.

4.2 Mean Flow Patterns and Power Number

The standard reactor vessel with $\frac{d}{D}$ of 2.90 and the reactor vessel with $\frac{d}{D}$ of 4.30 are considered for further

flow field analyses. The reactor vessel with $\frac{d}{D}$ of 4.30 is named as large reactor vessel hereafter in the further discussions. The mean flow pattern associated with the standard and large reactor vessels are illustrated in Figs. 4(a) and 4(b) respectively. The standard reactor vessel generates a double re-circulation pattern which comprises of two re-circulation loops above and below the impeller. High magnitudes of velocity can be observed near the impeller representing strong jet action of the discharge streams and significant magnitudes of velocity can be observed in the entire domain of the reactor vessel resulting in superior bulk mixing of the fluid contained within the reactor vessel. The strong jets emerging from the impeller propagates in a radial direction and strikes on the periphery of the reactor vessel to generate two re-circulation loops above and below the impeller. On the other hand, the large reactor vessel develops a single re-circulation pattern which consists of only two re-circulation loops within the reactor vessel. The strong jets emerging from the impeller move axially downwards and strike on the bottom surface of the reactor vessel to develop single re-circulation pattern within the reactor vessel. Since, the discharge streams move downwards, this flow pattern can also be named as single loop down-pumping pattern. Similar kind of single loop down-pumping pattern was also obtained by several researchers (Nienow, 1968; Montante et al., 1999, 2001) by keeping the RT impeller near the bottom surface of the standard reactor vessel. High magnitudes of velocity can be observed below the impeller up to the bottom surface of the large reactor vessel which provides superior localized mixing below the impeller surface. Moreover, two secondary circulation loops can be observed just below the impeller as well as near the air-water interface. The localized mixing near the bottom surface of the reactor vessel helps in lifting the fine solid particles off the bottom surface of the reactor vessel and suspending the same within the fluid contained within the reactor vessel. Thus, a transition from double re-circulation pattern to
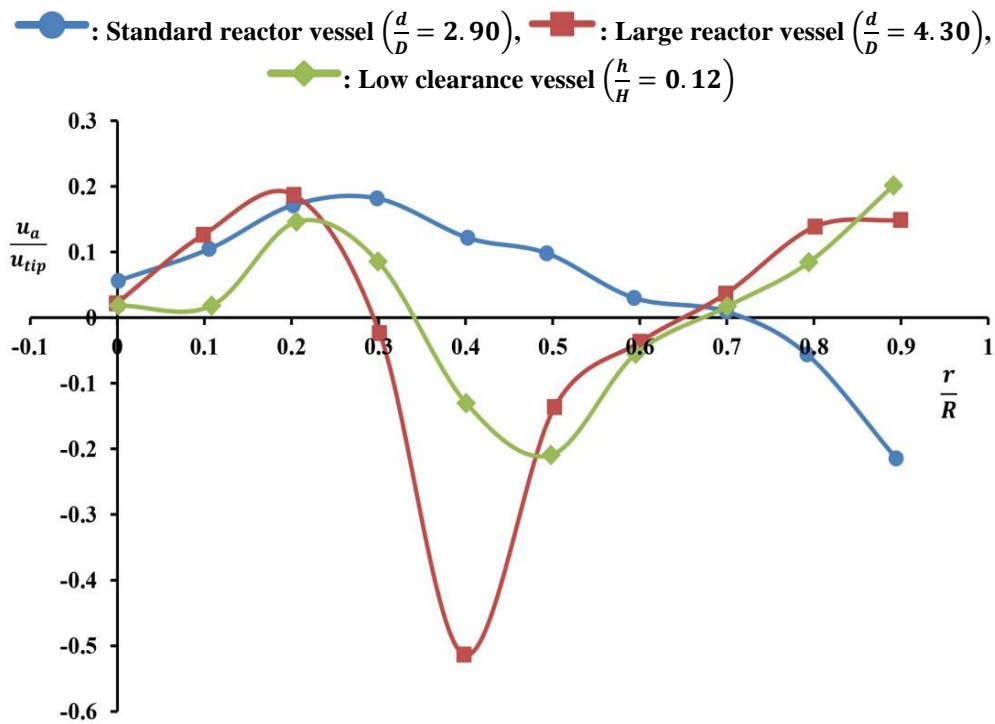
Fig. 5 Radial profile of $\frac{u_a}{u_{tip}}$ along a horizontal plane at $\frac{z}{d}$ of 0.28

single re-circulation pattern occurs with increase in the diameter of the reactor vessel apart from decrease in the clearance of the RT impeller as reported in the various research works of Nienow (1968), Montante et al. (1999) and Montante et al. (2001).

The flow pattern and N_{pt} associated with the standard reactor vessel from the present CFD model were compared against the same reported by Zhu et al. (2019). The formation of flow patterns in the reactor vessel is controlled by the underlying distribution of axial velocity fields (Montante et al., 1999). Therefore, the radial profiles of $\frac{u_a}{u_{tip}}$ along a horizontal plane at $\frac{z}{d}$ of 0.28 from the large reactor vessel, standard reactor vessel and low clearance vessel were compared as shown in Fig. 5 to analyse the differences in the flow patterns with variations in the $\frac{d}{D}$ of the reactor vessel. Zhu et al. (2019) have employed the low clearance vessel with $\frac{h}{H}$ of 0.12 and $\frac{d}{D}$ of 2.90 for the analysis purpose.

The standard reactor vessel has produced positive $\frac{u_a}{u_{tip}}$ up to a $\frac{r}{R}$ of 0.70 indicating the upward movement of flow while the $\frac{u_a}{u_{tip}}$ becomes negative further indicating the downward movement of the flow. These profiles represent the presence of re-circulation loops above and below the impeller and hence this flow pattern is known as double loop pattern. On the other hand, the large reactor vessel develops a different kind of axial velocity distribution in which the directions of axial velocities at most of the points in the radial profile were reversed as compared to the standard reactor vessel. The positive values of $\frac{u_a}{u_{tip}}$ were obtained for the $\frac{r}{R}$ between 0-0.30 indicating the upward movement of flow while the $\frac{u_a}{u_{tip}}$

values became negative for the $\frac{r}{R}$ between 0.30-0.60 indicating the downward movement of the flow. Thereafter, the $\frac{u_a}{u_{tip}}$ becomes positive for the $\frac{r}{R}$ more than 0.60 indicating the upward movement of the flow. These axial velocity profiles represent the presence of a single re-circulation loop in the vessel and therefore the corresponding flow pattern is regarded as single loop down-pumping pattern. Thus, the axial velocity distribution and in turn the flow pattern associated with the large reactor vessel is much different from the standard reactor vessel. This fact has much implication on the mixing applications of the standard and large reactor vessels. The double loop pattern associated with the standard reactor vessel is suitable for bulk mixing and dispersion applications while the single loop pattern related with the low clearance vessel is suitable for the solid-liquid suspension process.

The radial profile of $\frac{u_a}{u_{tip}}$ produced by the low clearance vessel follows the same trend as that provided by the large reactor vessel. However, the magnitudes of $\frac{u_a}{u_{tip}}$ associated with the large reactor vessel were higher than that produced by the low clearance vessel in the majority of the locations in the radial profile considered for the analysis. The peak positive $\frac{u_a}{u_{tip}}$ from large reactor vessel is 21.84% more than that produced by the low clearance vessel. Similarly, the peak negative $\frac{u_a}{u_{tip}}$ from the large reactor vessel is 59.25% more than that generated by the low clearance vessel. The strong axial pumping associated with the large reactor vessel makes it much suitable for the solid-liquid suspension process as compared to the low clearance vessel.

: N_{pt} from present study, □: Zhu et al. (2019)
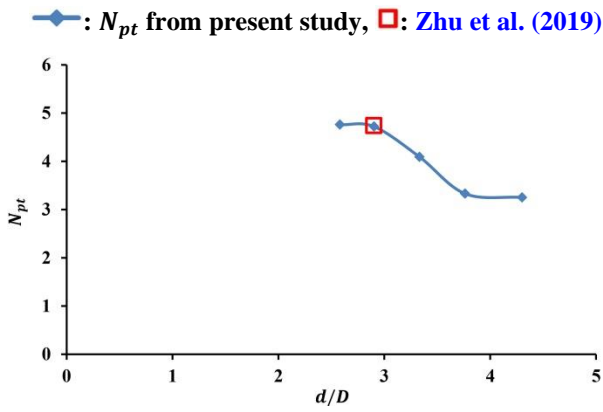
Fig. 6 Variation of N_{pt} with $\frac{d}{D}$ of the reactor vessel

The variation of N_{pt} with the $\frac{d}{D}$ of the reactor vessel is shown in Fig. 6. It is clear from Fig. 6 that the N_{pt} significantly decreases with increase in the $\frac{d}{D}$ of the reactor vessel. The large reactor vessel provides 31.14% reduction in the N_{pt} as compared to the standard reactor vessel. The N_{pt} of the standard reactor vessel predicted from the present study is same as that reported by Zhu et al. (2019) for the same configuration. On the other hand, reactor vessels with $\frac{d}{D}$ of 2.58 and 2.90 as well as reactor vessels with $\frac{d}{D}$ of 3.76 and 4.30 develop almost similar predictions of N_{pt}. Therefore, substantial difference exists in the prediction of N_{pt} between standard and large reactor vessels. In order to justify the decreasing trend of the power curve within the range of $\frac{d}{D}$ between 2.90 and 3.76, an additional CFD simulation corresponding to the vessel having $\frac{d}{D}$ of 3.33 was performed. The N_{pt} corresponding to the tank having $\frac{d}{D}$ of 3.33 is 13.35% lesser than that from the $\frac{d}{D}$ of 2.90 and 18.62% more than that from the $\frac{d}{D}$ of 3.76 respectively. These inferences again illustrate the continuous decrease in the N_{pt} with increase in the $\frac{d}{D}$ of the reactor vessel. Therefore, the decreasing trend of N_{pt} with increase in the $\frac{d}{D}$ of the reactor vessel is confirmed with the additional CFD simulation corresponding to the vessel having $\frac{d}{D}$ of 3.33. Further, the prediction of N_{pt} related with the large reactor vessel is almost same as that provided by the low clearance vessel $\left(\frac{h}{H} = 0.11\right)$. Hence, the large reactor vessel can be employed for the solid-liquid suspension process due to the development of high magnitudes of axial velocity as compared to the low clearance vessel at the same N_{pt}. The $\frac{d}{D}$ in the range between 2.90 and 3.76 can be considered as the critical range of tank diameter for the double to single loop pattern transition as the N_{pt} significantly decreases in this particular range of $\frac{d}{D}$. The significant decrease in the N_{pt} of the reactor vessel is an excellent indicator of the double loop to single loop pattern transition as reported by various research scholars

such as Montante et al. (1999) and Montante et al. (2001).

4.3 Hydrodynamic Reasons Causing Flow Pattern Transition and Reduction in N_{pt} with $\frac{d}{D}$

The hydrodynamic reasons causing double loop to single loop pattern transition and reduction in N_{pt} with $\frac{d}{D}$ are studied using the contours of mean pressure and trailing vortex structures respectively. The trailing vortices emerging from the rear side of the impeller blades were represented using the contours of Q-criterion (Huang & Green, 2015) as indicated in the Eq. (15).

The pressure within the reactor vessel is represented as pressure coefficient $\left(C_p\right)$ as defined in the Eq. (16).

$$Q = \frac{1}{2}(\|w\|^2 - \|S\|^2) \tag{15}$$

Where $\|w\|$ represents the Euclidean norm of rotation rate tensor and $\|S\|$ indicates the Euclidean norm of strain rate tensor respectively. The formation of a vortex is inferred when $Q > 0$, ie, the rotation rate of a fluid element dominates over the respective strain rate.

$$C_p = \frac{p}{\frac{1}{2}\rho_q u_{tip}^2} \tag{16}$$

Where u_{tip} is the impeller tip velocity.

The contours of C_p along the mid-baffle plane of the standard reactor vessel and large reactor vessel are shown in Figs. 7(a) and 7(b) respectively. The standard reactor vessel produces high pressure near the impeller and uniform distribution of pressure in the remaining domain of the reactor vessel resulting in the formation of radial discharge streams and double loop pattern within the reactor vessel. On the other hand, large reactor vessel develops a distinct low pressure region below the impeller which drags the discharge streams axially downwards and strikes on the bottom surface of the reactor vessel to provide single loop down-pumping pattern within the reactor vessel. Thus, the pressure distribution around the impeller controls the flow pattern developed within the reactor vessel.

The contours of trailing vortices along the centre-plane of the RT impeller of the standard reactor vessel and large reactor vessel are shown in Figs. 8(a) and 8(b) respectively. The contours of trailing vortices along the mid-baffle plane for the standard reactor vessel and large reactor vessel are shown in Figs. 9(a) and 9(b) respectively. The standard reactor vessel generates a symmetric pair of trailing vortices above and below the impeller centre-plane which propagate radially towards the periphery of the reactor vessel (Fig. 9(a)). The radial movement of trailing vortices provides larger zone of vortex action behind the impeller blades (Fig. 8(a)) which increases the strength of flow separation regions associated with the impeller. The stronger flow separation regions decrease the pressure on the suction side of the blades resulting in high pressure difference between the suction and pressure sides of the blades. The high pressure difference between the suction and pressure sides of the blades increases the form drag and
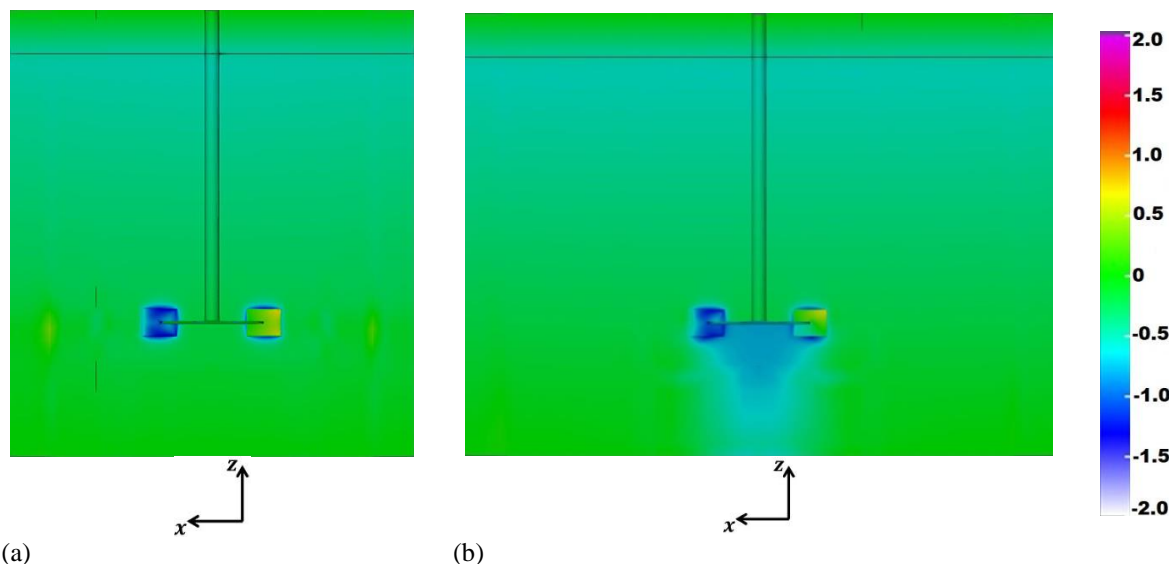
Fig. 7 Contours of C_p along the mid-baffle plane associated with the $\frac{d}{D}$ of (a) 2.90 and (b) 4.30 (Black line in figures indicates air-water interface before the commencement of simulations)
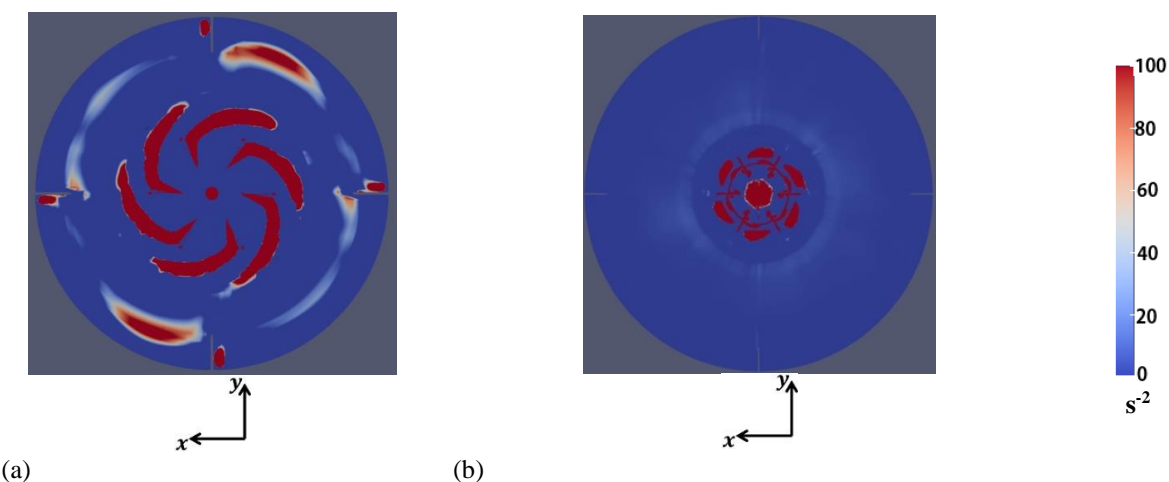
Fig. 8 Contours of trailing vortices along the impeller centre-plane associated with $\frac{d}{D}$ of (a) 2.90 and (b) 4.30
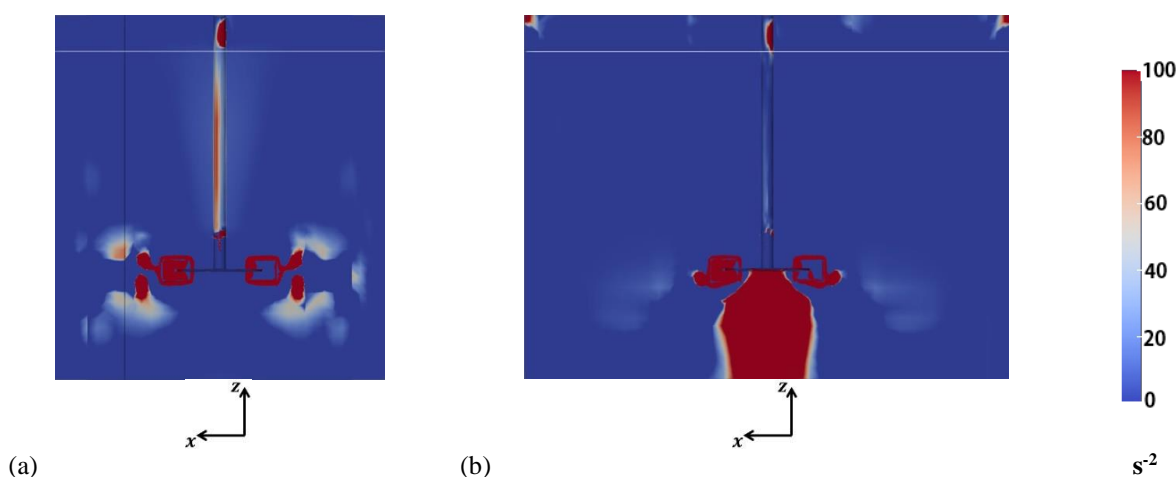
Fig. 9 Contours of trailing vortices along the mid-baffle plane associated with $\frac{d}{D}$ of (a) 2.90 and (b) 4.30 (White line in figures indicates air-water interface before the commencement of simulations)

torque of the RT impeller. The high impeller torque in turn results in high N_{pt} associated with the RT impeller. On the other hand, the down-pumping discharge streams associated with the large reactor vessel causes downward movement of trailing vortex structures from the bottom corners of the impeller blades (Fig. 9(b)). Moreover, trailing vortex structures are not generated and propagated from the top corners of the impeller blades
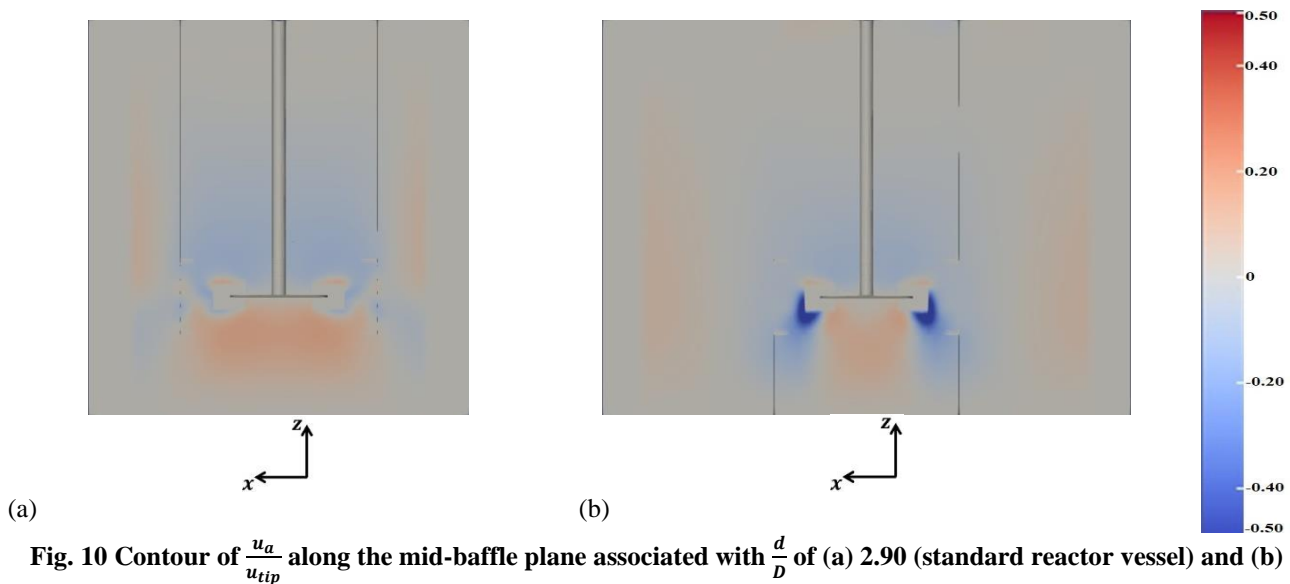
Fig. 10 Contour of $\frac{u_a}{u_{tip}}$ along the mid-baffle plane associated with $\frac{d}{D}$ of (a) 2.90 (standard reactor vessel) and (b) 4.30

(Fig. 9(b)). The downward movement of trailing vortices produces smaller zone of vortex action behind the impeller blades (Fig. 8(b)) which in turn decreases the strength of flow separation regions associated with the impeller. The weaker flow separation regions increase the pressure on the suction sides of the impeller blades resulting in smaller pressure difference between the suction and pressure sides of the impeller blades. The smaller pressure difference between the suction and pressure sides of the impeller blades leads to smaller form drag and torque associated with the RT impeller. The small impeller torque eventually results in small N_{pt} associated with the impeller. Thus, the distribution of trailing vortices surrounding the impeller blades controls the N_{pt} of the reactor vessel.

4.4 Suitability of Large Reactor Vessel for Solid-Liquid Suspension Process

The present sub-section focuses on the assessment of suitability of large reactor vessels for the suspension of solid particles in the liquid contained within the reactor vessel. The contours of $\frac{u_a}{u_{tip}}$ along the mid-baffle plane associated with standard and large reactor vessels are shown in Figs. 10(a) and 10(b) respectively. As shown in Fig. 10(b), negative $\frac{u_a}{u_{tip}}$ near the impeller blades of large reactor vessel causes downward movement of discharge streams and positive $\frac{u_a}{u_{tip}}$ near the bottom surface of the large reactor vessel leads to the upward movement of the same. This flow pattern is suitable for suspending the solid particles in the liquid (Nienow, 1968; Montante et al., 1999; Zhu et al., 2019) contained in the large reactor vessel and termed as single loop pattern earlier. Moreover, positive $\frac{u_a}{u_{tip}}$ present below the impeller provides upward flow from the bottom surface of the large reactor vessel. This in turn prevents the settling of solid particles in the bottom surface of the large reactor vessel. On the other hand, the positive $\frac{u_a}{u_{tip}}$ below the impeller and negative $\frac{u_a}{u_{tip}}$ above the impeller of standard reactor vessel as shown in Fig.

10(a) results in double loop pattern which is suitable for bulk mixing of the fluid contained in the reactor vessel. Moreover, high magnitude of $\frac{u_a}{u_{tip}}$ below the impeller of large reactor vessel as compared to the low clearance vessel (Fig. 5) at the same N_{pt} makes the former reactor configuration more suitable for the solid-liquid suspension process than the latter reactor configuration.

In addition to the axial velocity fields and re-circulation patterns, vortex and turbulence activity of the standard and large reactor vessels were analysed using the contours of trailing vortices and normalized turbulent kinetic energy $\left(\frac{k}{u_{tip}^2}\right)$ respectively. As shown in Fig. 9(b), trailing vortices were developed only from the bottom corners of the blades which move towards the bottom surface of the large reactor vessel. Moreover, superior vortex activity can be observed below the impeller up to bottom surface of the reactor large vessel. Similarly, high magnitudes of $\frac{k}{u_{tip}^2}$ can be observed below the bottom part of the impeller blades which extend up to the bottom surface of the reactor vessel as depicted in Fig. 11. The trailing vortices and turbulence fields follow the trajectory of down-pumping discharge streams and produces localized mixing below the impeller up to the bottom surface of the reactor vessel. The inferior vortex activity around the RT impeller of large reactor vessel as obtained from the study of Van Der Molen and Van Maanen (1978) might be due to the downward movement of trailing vortices and effective dissipation of the same near the bottom surface of the reactor vessel. Thus, the large reactor vessel develops high vortex and turbulence activity below the impeller up to the bottom surface of the reactor vessel which helps in lifting the solid particles upwards and suspending the same in the liquid contained within the reactor vessel. On the other hand, the standard reactor vessel provides symmetric trailing vortices above and below the impeller centre-plane (Fig. 9(a)) and superior vortex and turbulence activity in the entire domain of the reactor vessel (Figs. 9(a) and 11(a)).
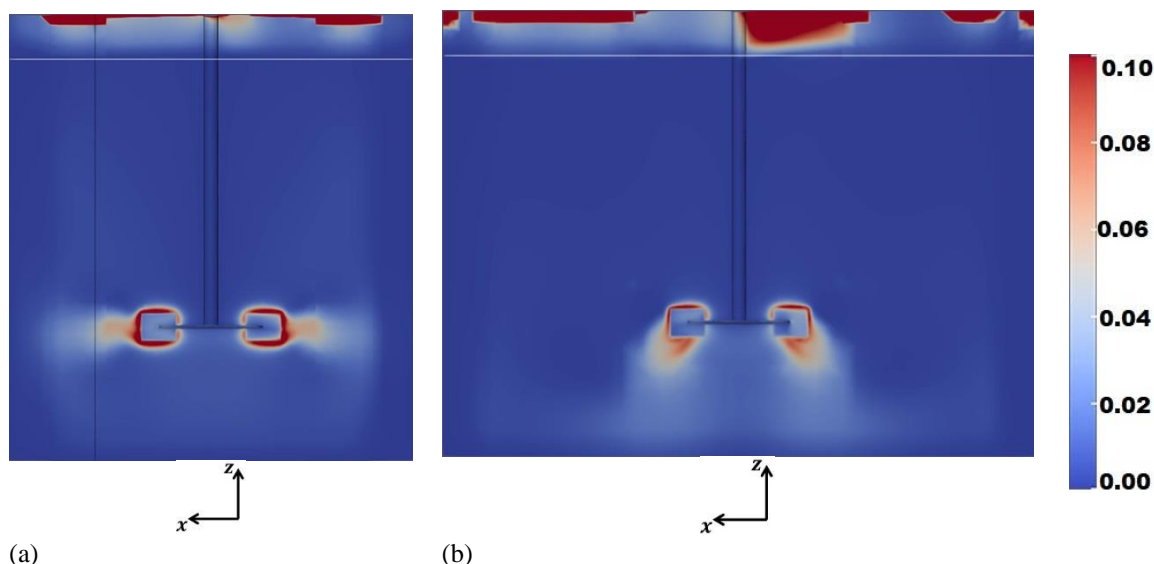
Fig. 11 Contours of $\frac{k}{u_{tip}^2}$ along the mid-baffle plane associated with $\frac{d}{D}$ of (a) 2.90 and (b) 4.30 (White line in figures indicates the air-water interface before the commencement of simulations)

The significant vortex and turbulence action in the entire domain of the vessel results in bulk mixing of the fluid contained within the reactor vessel.

Apart from these features, variation of gas hold-up with $\frac{d}{D}$ of the reactor vessel was analysed as shown in Fig. 12. The gas hold-up slightly increased with increase in the $\frac{d}{D}$ of the reactor vessel. The standard reactor vessel and reactor vessel with $\frac{d}{D}$ of 3.76 provided similar gas hold-up values which increased only by 12% with increase in $\frac{d}{D}$ to 4.30. Thus, the large reactor vessel doesn't provide excessive entrainment of air into the liquid which is again a favourable condition for the solid-liquid suspension process as specified by Nienow (1968).

In general, large reactor vessels are suitable for the solid-liquid suspension process due to the formation of single loop down-pumping pattern, appropriate distribution of $\frac{u_a}{u_{tip}}$, superior vortex and turbulence action below the impeller up to the bottom surface of the reactor vessel and inferior entrainment of air into the liquid contained within the reactor vessel.
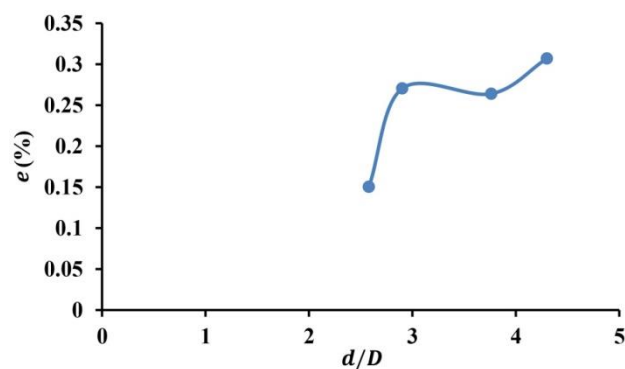
Since, the reactor vessels with large diameter are found suitable for the solid-liquid suspension process, detailed experiments can be taken-up in future to analyse its mixing characteristics (i.e., mixing time, mixing energy, speed and time for complete suspension of particles) and effect of various geometric parameters (i.e., impeller diameter, impeller speed, number of blades of impeller and number of baffle walls) on the underlying flow field characteristics and mixing performance. Also, experiments and CFD simulations can be conducted in a wide spectrum of $\frac{d}{D}$ so as to fix appropriate range of $\frac{d}{D}$ for large reactor vessels, range of $\frac{d}{D}$ within which flow pattern transition occurs and impacts of other vessel parameters on the performance features. This in turn makes the conclusions more general which will be beneficial to the industrial practitioners and research community.

In addition to the solid-liquid suspension process, the large reactor vessels can be adopted as pump-mix mixers in the nuclear industries as the underlying single loop down-pumping pattern as well as superior vortex and turbulence activity near the bottom surface of such vessels fulfills the allied pumping and mixing requirements. Moreover, the above mentioned flow features of large reactor vessels are also suitable for ion exchange and dissolution processes related with the chemical and process industries. Further, the large reactor vessel can be used for suspending the catalysts in the reagents for various chemical reactions in which the top layer of the liquid may contain few particles or sometimes no any solid particles.

5. CONCLUSIONS

The mean and turbulent flow fields associated with the baffled reactor vessels having different diameter agitated using the RT impeller were analysed using the CFD technique so as to assess the suitability of large reactor vessels for the solid-liquid suspension process.

Fig. 12 Variation of gas hold-up with $\frac{d}{D}$

The Reynolds stress terms were modelled using the standard $k - \varepsilon$ model and the impeller baffle interactions were simulated using the MRF method. The $\frac{d}{D}$ was varied in the range between 2.58 to 4.30. The increase in $\frac{d}{D}$ from standard configuration of the reactor vessel causes the transition from double loop pattern to single loop down-pumping pattern. Moreover, the N_{pt} was significantly decreased with increase in the $\frac{d}{D}$ of the reactor vessel.

The increase in $\frac{d}{D}$ causes the formation of a low pressure region below the impeller which deflects the discharge streams towards the bottom surface of the reactor vessel leading to the development of single loop down-pumping pattern within the reactor vessel. The downward movement of trailing vortices present in the discharge streams decreases the strength of flow separation regions behind the impeller blades which in turn reduces the form drag and power number of the impeller.

The downward movement of trailing vortices and turbulence fields from the impeller led to superior localized mixing effects below the impeller up to the bottom surface of the reactor vessel. High magnitudes of $\frac{u_a}{u_{tip}}$ were observed below the impeller up to bottom surface of the vessel which is appropriate for the solid-liquid suspension process. Moreover, negligible increase of gas hold-up was obtained with increase in the $\frac{d}{D}$ of the reactor vessel. Thus, the formation of single loop pattern, downward movement of discharge streams and trailing vortices, negligible gas hold-up, superior localized mixing below the impeller up to bottom surface of the reactor vessel and appropriate distribution of axial velocity magnitudes make the large reactor vessels suitable for the solid-liquid suspension process. Moreover, the large reactor vessel developed high magnitudes of axial velocity fields above and below the impeller as compared to the low clearance vessel at the same N_{pt}. Hence, the large reactor vessel is much suited for the solid-liquid suspension process as compared to the low clearance vessel.

The development of hydrodynamic characteristics appropriate for the solid-liquid suspension process with less N_{pt} increases the possibilities of extensive usage of the large reactor vessels in the chemical and related industries. Apart from the solid-liquid suspension process, the large reactor vessels can be used as pump-mix mixers in the nuclear industry and for ion exchange and dissolution processes related with the chemical and process industries. Moreover, the insignificant wear and tear of impeller blades associated with the large reactor vessels avoids the huge maintenance cost which in turn increases its acceptability among the various industries. The low clearance vessels which are widely used for the solid-liquid suspension process significantly increases the maintenance cost due to wear and tear of impeller blades although the performance of the same is similar to the large reactor vessels.

CONFLICT OF INTEREST

The authors have no relevant financial or non-financial interests to disclose.

AUTHORS CONTRIBUTION

Devarajan Krishna Iyer: Conceptualization, Methodology, Validation, Formal analysis, Writing-Original Draft, Visualization

Ajey Kumar Patel: Conceptualization, Resources, Writing- Review & Editing, Supervision, Project administration, Funding acquisition

REFERENCES

Alcamo, R., Micale, G., Grisafi, F., Brucato, A., & Ciofalo, M. (2005). Large-eddy simulation of turbulent flow in an unbaffled stirred tank driven by a Rushton turbine. *Chemical Engineering Science*, *60*(8–9), 2303–2316. https://doi.org/10.1016/j.ces.2004.11.017

Alonzo-Garcia, A., Mendoza-Escamilla, V. X., Martinez-Delgadillo, S. A., Gonzalez-Neria, I., Del C Gutiérrez-Torres, C., & Jiménez-Bernal, J. A. (2019). On the performance of different rans based models to describe the turbulent flow in an agitated vessel using non-structured grids and PIV validation. *Brazilian Journal of Chemical Engineering*, *36*(1), 361–382. https://doi.org/10.1590/0104-6632.20190361s20180091

ANSYS, I. (2013). *ANSYS fluent theory guide* (Release, 1). ANSYS.

Armenante, P. M., & Nagamine, E. U. (1998). Effect of low off-bottom impeller clearance on the minimum agitation speed for complete suspension of solids in stirred tanks. *Chemical Engineering Science*, *53*(9), 1757–1775. https://doi.org/10.1016/S0009-2509(98)00001-3

Armenante, P. M., Nagamine, E. U., & Susanto, J. (1998). Determination of Correlations to Predict the Minimum Agitation Speed for Complete Solid Suspension in Agitated Vessels. *The Canadian Journal of Chemical Engineering*, *76*, 413–419. https://doi.org/10.1002/cjce.5450760310

Başbuğ, S., Papadakis, G., & Vassilicos, J. C. (2018). Reduced power consumption in stirred vessels by means of fractal impellers. *AIChE Journal*, *64*(4), 1485–1499. https://doi.org/10.1002/aic.16096

Bates, R. L., Fondy, P. L., & Corpstein, R. R. (1963). Examination of some geometric parameters of

impeller power. *Industrial & Engineering Chemistry Process Design and Development*, *2*(4), 310–314. https://doi.org/10.1021/i260008a011

Celik, B., Ghia, U., Roache, P. J., Freitas, C. J., Coleman, H., & Raad, P. E. (2008). Procedure for estimation and reporting of uncertainty due to discretization in CFD applications. *Journal of Fluids Engineering*, *130*(7), 078001. https://doi.org/10.1115/1.2960953

Conti, R., Sicardi, S., & Specchia, V. (1981). Short communication. *The Chemical Engineering Journal*, *22*, 247–249. https://doi.org/10.1080/10236240210000193333

Coroneo, M., Montante, G., Paglianti, A., & Magelli, F. (2011). CFD prediction of fluid flow and mixing in stirred tanks: Numerical issues about the RANS simulations. *Computers & Chemical Engineering*, *35*(10), 1959–1968. https://doi.org/10.1016/j.compchemeng.2010.12.007

Deglon, D. A., & Meyer, C. J. (2006). CFD modelling of stirred tanks: Numerical considerations. *Minerals Engineering*, *19*(10), 1059–1068. https://doi.org/10.1016/j.mineng.2006.04.001

Freitas, C. J. (2002). The issue of numerical uncertainty. *Applied Mathematical Modelling*, *26*(2), 237–248. https://doi.org/10.1016/S0307-904X(01)00058-0

Galletti, C., Brunazzi, E., Yianneskis, M., & Paglianti, A. (2003). Spectral and wavelet analysis of the flow pattern transition with impeller clearance variations in a stirred vessel. *Chemical Engineering Science*, *58*(17), 3859–3875. https://doi.org/10.1016/S0009-2509(03)00230-6

Harriott, P. (1962). Mass transfer to particles: Part I. Suspended in agitated tanks. *AIChE Journal*, *8*(1), 93–101. https://doi.org/10.1002/aic.690080122

Hirt, C. W., & Nicholas, B. D. (1981). Volume of fluid method for the dynamics of free surface boundaries. *Journal of Computational Physics, 39*, 201-225. https://doi.org/10.1016/0021-9991(81)90145-5

Huang, Y., & Green, M. A. (2015). Detection and tracking of vortex phenomena using Lagrangian coherent structures. *Experiments in Fluids*, *56*(7), 1-12. https://doi.org/10.1007/s00348-015-2001-z

Iyer, D. K., & Patel, A. K. (2022). Physical Reasoning of Double- to Single-Loop Transition in Industrial Reactors using Computational Fluid Dynamics. *J. Appl. Fluid Mech.*, *15* (5), 1621-1634. https://doi.org/10.47176/jafm.15.05.1190.

Jirout, T., & Jiroutová, D. (2020). Application of theoretical and experimental findings for optimization of mixing processes and equipment. *Processes*, *8*(955), 1-25. https://doi.org/10.3390/pr8080955

Joshi, J. B., Nere, N. K., Rane, C. V., Murthy, B. N., Mathpati, C. S., Patwardhan, A. W., & Ranade, V. V. (2011). CFD simulation of stirred tanks: Comparison of turbulence models. Part I: Radial flow impellers.

The Canadian Journal of Chemical Engineering, *89*(1), 23–82. https://doi.org/10.1002/cjce.20446

Karpinska, A. M., & Bridgeman, J. (2018). CFD as a tool to optimize aeration tank design and operation. *Journal of Environmental Engineering*, *144*(2), 05017008 1-12. https://doi.org/10.1061/(ASCE)EE.1943-7870.0001307

Kolář, V. (1961). Studies on mixing. X. Suspending solid particles in liquids by means of mechanical agitation. *Collection of Czechoslovak Chemical Communications*, *26*(3), 613–627. https://doi.org/10.1135/cccc19610613

Li, Z., Bao, Y., & Gao, Z. (2011). PIV experiments and large eddy simulations of single-loop flow fields in Rushton turbine stirred tanks. *Chemical Engineering Science*, *66*(6), 1219–1231. https://doi.org/10.1016/j.ces.2010.12.024

Longest, P. W., & Vinchurkar, S. (2007). Effects of mesh style and grid convergence on particle deposition in bifurcating airway models with comparisons to experimental data. *Medical Engineering & Physics*, *29*(3), 350–366. https://doi.org/10.1016/j.medengphy.2006.05.012

Montante, G., Brucato, A., Lee, K. C., & Yianneskis, M. (1999). An experimental study of double-to-single-loop transition in stirred vessels. *The Canadian Journal of Chemical Engineering*, *77*(4), 649–659. https://doi.org/10.1002/cjce.5450770405

Montante, G., Lee, K. C., Brucato, A., & Yianneskis, M. (2001). Numerical simulations of the dependency of flow pattern on impeller clearance in stirred vessels. *Chemical Engineering Science*, *56*(12), 3751–3770. https://doi.org/10.1016/S0009-2509(01)00089-6

Nienow, A. W. (1968). Suspension of solid particles in turbine agitated baffled vessels. *Chemical Engineering Science*, *23*(12), 1453-1459. https://doi.org/10.1080/02726358708904551

Oberkampf, W. L., & Trucano, T. G. (2002). Verification and validation in computational fluid dynamics. *Progress in Aerospace Sciences*, *38*(3), 209–272. https://doi.org/10.1016/S0376-0421(02)00005-2

Ochieng, A., & Onyango, M. S. (2008). Homogenization energy in a stirred tank. *Chemical Engineering and Processing: Process Intensification*, *47*(9–10), 1853–1860. https://doi.org/10.1016/j.cep.2007.10.014

Ochieng, A., Onyango, M. S., Kumar, A., Kiriamiti, K., & Musonge, P. (2008). Mixing in a tank stirred by a Rushton turbine at a low clearance. *Chemical Engineering and Processing: Process Intensification*, *47*(5), 842–851. https://doi.org/10.1016/j.cep.2007.01.034

Sepro mixing & pumping. (2022, August 20). *Mixing fundamentals: solids suspension.* 101A-9850 201 Street, Langley, British Columbia VIM 4A3, Canada. https://mixing.seprosystems.com

Van Der Molen, K., & Van Maanen, H. R. E. (1978). Laser-Doppler measurements of the turbulent flow in stirred vessels to establish scaling rules. *Chemical Engineering Science*, *33*(9), 1161–1168. https://doi.org/10.1016/0009-2509(78)85081-7

Vinchurkar, S., & Longest, P. W. (2008). Evaluation of hexahedral, prismatic and hybrid mesh styles for simulating respiratory aerosol dynamics. *Computers & Fluids*, *37*(3), 317–331. https://doi.org/10.1016/j.compfluid.2007.05.001

Wu, H., & Patterson, G. K. (1989). Laser-Doppler measurements of turbulent-flow parameters in a stirred mixer. *Chemical Engineering Science*, *44*(10), 2207–2221. https://doi.org/10.1016/0009-2509(89)85155-3

Yapici, K., Karasozen, B., Schäfer, M., & Uludag, Y. (2008). Numerical investigation of the effect of the Rushton type turbine design factors on agitated tank flow characteristics. *Chemical Engineering and Processing: Process Intensification*, *47*(8), 1340–1349. https://doi.org/10.1016/j.cep.2007.05.002

Zhu, Q., Xiao, H., Chen, A., Geng, S., & Huang, Q. (2019). CFD study on double- to single-loop flow pattern transition and its influence on macro mixing efficiency in fully baffled tank stirred by a Rushton turbine. *Chinese Journal of Chemical Engineering*, *27*(5), 993–1000. https://doi.org/10.1016/j.cjche.2018.10.002

Zwietering, T. N. (1958). Suspending of solid particles in liquid by agitators. *Chemical Engineering Science*, *8*(3–4), 244–253. https://doi.org/10.1016/0009-2509(58)85031-9